

Simulating Ground-Motion Directivity Using Stochastic Empirical Green's Function Method

by Hongwei Wang, Ruizhi Wen, and Yefei Ren

Abstract First, strong-motion recordings from an M_w 4.4 earthquake with symmetrical rupture were regarded as empirical Green's functions (EGFs) to simulate ground motions produced by the 2013 M_w 6.6 Lushan mainshock using the two-step stochastic EGF method proposed by Kohrs-Sansorny *et al.* (2005). In this simulation, the source of the Lushan mainshock was set to consist only of an asperity in the vicinity of the hypocenter, which was determined according to the statistical properties of asperity. The good agreement between the simulated ground motions and the observed recordings at short periods (< 2.0 s) validates this method. Furthermore, recordings from an M_w 4.5 earthquake with significant rupture directivity were used as EGFs to simulate ground motions of the Lushan mainshock. The rupture directivity mainly exerts significant effects on the simulated short-period ground motions, which result in large discrepancies with the observed recordings. Simulated ground motions are much higher than the observed ones at directive stations, but lower at antidirective stations. More significant effects are observed at directive stations than antidirective stations. Using the azimuthal apparent corner frequency to consider the rupture directivity in the two-step stochastic EGF method, the good reproductions of the observed recordings are obtained at short periods, which indicates that the rupture directivity at short periods can be simulated well. Finally, ground motions from a series of Lushan-like earthquakes assuming various rupture directivities were simulated by adjusting the apparent corner frequency. The simulated ground motions show significant directivity effects. The two-step stochastic EGF method provides an effective approach to predicting ground motions for future earthquakes because far fewer source parameters are required.

Introduction

Predicting ground motion at a given site for a future earthquake is a major task for seismic-hazard assessment. The prediction mainly consists of two stages: the generation of seismic waves (the rupture process) and wave propagation (Green's function). There are two primary methods according to the acquisition of Green's function: theoretical and empirical Green's function methods. The theoretical Green's function method cannot effectively simulate the high-frequency ground motion owing to the lack of the precisely descriptions for the crustal structure and the rupture process (Zeng *et al.*, 1994; Olsen *et al.*, 1997). The empirical Green's function (EGF) method regards observed recordings in smaller earthquakes as Green's function for all points on the rupture plane of a larger earthquake (Hartzell, 1978). In general, EGF is the high signal-to-noise ratio recording observed in a smaller earthquake with an adjacent hypocenter and similar focal mechanism to the larger earthquake. Because actual properties of the source rupture and propagation medium are included in the EGF, high-frequency ground motions can be predicted well by the EGF method.

Compared with the classical EGF method, which is strongly dependent on the kinematic description of the rupture process on an extended rupture plane (Irikura, 1983; Irikura and Kamae, 1994), the stochastic EGF method is capable of generating many variable ground motions which correspond to a multitude of rupture processes and are, on average, in exact agreement with the well-known ω^{-2} model (Brune, 1970) in the whole frequency band (Joyner and Boore, 1986; Wennerberg, 1990; Ordaz *et al.*, 1995; Kohrs-Sansorny *et al.*, 2005). However, the stochastic EGF method is unable to account for possible directivity effects owing to the point-source hypothesis for the earthquake to be simulated (the target earthquake) (Ordaz *et al.*, 1995; Kohrs-Sansorny *et al.*, 2005). In fact, the predominance of unilateral ruptures in large earthquakes has been confirmed (McGuire *et al.*, 2002). Meanwhile, the persistence of directivity in small-to-moderate earthquakes has also been verified by analyzing the peak ground-motion parameters or the apparent source duration, such as the 11 May 2011 M_w 5.2 Lorca, Spain, earthquake (López-Comino *et al.*, 2012); three moderate

earthquakes (M 4.2, 4.9, and 5.4) in 2012 in northern Italy (Convertito and Emolo, 2012); seven $3.5 \leq M \leq 4.1$ earthquakes in November 2002 and February 2003 near San Ramon, California (Boatwright, 2007); and an M_w 4.1 earthquake in the French Alps (Couboulex *et al.*, 2013).

In general, a small earthquake is usually assumed as a point source. We are not concerned with the rupture process of a small earthquake or the effects of this rupture process on the ground motions. When we select appropriate recordings from small earthquakes as EGFs, the rupture processes of these earthquakes are certainly ignored. The rupture directivity of a small earthquake exposes a significant impact to high-frequency ground motions, which has been confirmed by observed recordings and theoretical studies (Bernard *et al.*, 1996; McGuire, 2004; Boatwright, 2007; Cultrera *et al.*, 2009; Couboulex *et al.*, 2013). In the study of Couboulex *et al.* (2010), the directivity effects of the rupture propagation of the small earthquake taken as EGF were raised to be an open problem for simulations.

Although the directivity effects for the target earthquake have been successfully simulated based on the composite source model or the k^{-2} kinematic source model (Bernard *et al.*, 1996; Galovic and Burjanek, 2007; Ruiz *et al.*, 2011), modeling the directivity effects not only for the larger earthquakes but also in the case of smaller earthquakes taken as EGF in the stochastic EGF method were investigated in few literature. Honore *et al.* (2011) simulated ground motions produced by an M_w 4.5 earthquake with the rupture directivity using different corner frequencies between the rupture direction and the opposite direction in the stochastic EGF method. Therefore, effectively simulating the directivity effect is still a stringent problem in the stochastic EGF method.

An M_w 6.6 earthquake hit Lushan County, China, on 20 April 2013. The kinematic source rupture models were constrained by inverting or jointly inverting waveforms of teleseismic broadband body waves, strong motions, and long-period surface waves. These results indicate that the Lushan mainshock is a shallow interplate blind-thrust earthquake showing no significant directivity where the fault slips are mainly concentrated on the hypocenter (Hao *et al.*, 2013; Wang *et al.*, 2013; Zhang *et al.*, 2013, 2014).

In this article, we first simulated ground motions of the 2013 M_w 6.6 Lushan mainshock using the two-step stochastic EGF method proposed by Kohrs-Sansornny *et al.* (2005) to test the validity of this method. Strong-motion recordings from an M_w 4.4 earthquake, which was confirmed to have no rupture directivity, were regarded as EGFs. The source of the Lushan mainshock was set to include only an asperity, which was determined according to the statistical properties of the asperity. Furthermore, strong-motion recordings obtained in an M_w 4.5 earthquake with significant rupture directivity were used as EGFs to investigate the rupture directivity effects on the simulated ground motions of the Lushan mainshock. The azimuthal apparent corner frequency was adopted in the two-step stochastic EGF method

to simulate the rupture directivity. Finally, a preliminary attempt was made to simulate the directivity effects of a series of M_w 6.6 Lushan-like earthquakes with different rupture directivities.

Methods

In this study, we used the two-step stochastic EGF method proposed by Kohrs-Sansornny *et al.* (2005). This method requires fewer input parameters, only including the seismic moment and the stress-drop ratio. Compared with the single-step stochastic EGF methods (Wennerberg, 1990; Ordaz *et al.*, 1995), more realistic and sufficiently different ground motions can be generated by the two-step stochastic EGF method. Moreover, a study has proved the validity and stability of this method in simulating the ground motions produced by an M_w 6.4 earthquake (Couboulex *et al.*, 2010).

The simulated ground motion $S(t)$ can be represented as the convolution between the equivalent source time function $ESTF(t)$ and the recording $s(t)$ from a small earthquake. In the two-step stochastic EGF method proposed by Kohrs-Sansornny *et al.* (2005), $ESTF(t)$ is generated in two steps. In the first step, a number η_c of time delays t_c are randomly generated following a probability density function $\rho_c(t)$ over the source duration T_c . T_c is equal to the inverse of the corner frequency F_c . In the second step, a number η_d of time delays t_d are again randomly generated following the other probability density function $\rho_d(t)$ over a window duration $T_d \leq T_c$, which is centered on each time delay generated in the first step. Finally, $\eta = \eta_c \eta_d$ small events are summed together and scaled by a factor κ :

$$ESTF_i(t) = \kappa \sum_{d=1}^{\eta_d} \sum_{c=1}^{\eta_c} \delta[t - t_c(i) - t_d(i)]. \quad (1)$$

Under the conditions of exact agreement between the ratio of the simulated ground motion averaged over all realizations to the recording as EGF from the smaller earthquake in the frequency domain and the ω^{-2} spectral ratio of the larger earthquake to the smaller earthquake (Brune, 1970), and the self-similarity of the earthquake (Kanamori and Anderson, 1975), η and κ are expressed as

$$\eta = \eta_c \eta_d = N^4, \quad \kappa = C/N, \quad (2)$$

in which $N = f_c/F_c$, $C = \Delta\Sigma/\Delta\sigma$, and $CN^3 = M_0/m_0$. $F_c(f_c)$, $\Delta\Sigma(\Delta\sigma)$, and $M_0(m_0)$ are the corner frequency, stress drop, and seismic moment for a larger (smaller) earthquake, respectively. In this article, $\eta_c = \eta_d = N^2$. Following Brune (1970), the corner frequency can be given by the equation $F_c = 4.9 \times 106\beta(\Delta\Sigma/M_0)1/3$, in which β is the shear-wave velocity set to 3.6 km/s. The probability density functions were expressed in detail by Kohrs-sansornny *et al.* (2005) in their appendix A.

The stress drop is linked to the dynamics of the source rupture and hence also to the associated energy release and

Table 1
Basic Information for the Lushan Mainshock and Three Aftershocks

Event	Data (yyyy/mm/dd)	Time (UTC) (hh:mm:ss)	M_w	Hypocenter Location			Focal Mechanisms			Rupture Parameters		
				Longitude (°)	Latitude (°)	Depth (km)	Strike (°)	Dip (°)	Rake (°)	φ	v_r/β	k
Lushan mainshock	2013/04/20	00:02:46	6.6	102.97	30.30	14	209	46	94	—	—	—
EQI	2013/04/20	01:02:58	4.4	102.87	30.27	18	186	19	81	204.5	0.62	0.52
EQII	2013/04/20	03:34:17	5.0	102.89	30.19	14	212	50	98	214.2	0.61	0.80
EQIII	2013/04/20	20:53:44	4.5	103.03	30.35	16	200	30	106	206.5	0.69	0.89

M_w , moment magnitude; φ , rupture direction; v_r , rupture velocity; β , shear-wave velocity; k , rupture proportion in direction φ .

seismic radiation. Methods for measuring the averaged stress drop over the entire fault plane were summarized in the review article of [Kanamori \(1994\)](#). In general, the average stress drop can be computed from the measured seismic moment and rupture area. The stress drop estimated for global earthquake catalogs varies in a very wide range, approximately from 0.1 to 100 MPa ([Allmann and Shearer, 2009](#); [Zhao et al., 2011](#); [Courboux et al., 2016](#)). If we focus on a future earthquake or historical earthquake, it is difficult to measure or estimate the stress drop. However, many relationships between the seismic moment and the rupture area have been developed (e.g., [Wells and Coppersmith, 1994](#); [Somerville et al., 1999](#); [Hanks and Bakun, 2002](#); [Irikura et al., 2004](#); [Murotani et al., 2015](#), etc.), in which the three-stage scaling relationship proposed by [Irikura et al. \(2004\)](#) was more appropriate for the observational fact ([Fujii and Matsuura, 2000](#); [Shaw and Scholz, 2001](#)). On the basis of the relationship of [Irikura et al. \(2004\)](#), the average stress drop implied from the dynamic rupture simulations undergoes three stages, in which it first remains constant and then increases linearly and finally maintains a constant with the increase in the aspect ratio of the fault plane (the ratio of the fault length to the fault width) ([Irikura et al., 2004](#); [Dalguer et al., 2008](#)).

The distribution of the stress drop on the fault plane is highly heterogeneous because of the nonuniform stress or strength distribution. High-frequency ground motions are mainly contributed by the relatively high stress-drop regions on the fault plane, which spatially coincide well with the asperities ([Miyake et al., 2003](#)). The area outside the asperities predominates the low-frequency ground motions. [Somerville et al. \(1999\)](#) defined the asperity as area whose slip is 1.5 or more times larger than the average slip over the fault plane, and developed its statistical characteristics. [Kamae and Kawabe \(2004\)](#) succeeded in simulating ground motions produced by the 2003 M_{JMA} 8.0 Tokachi-Oki earthquake assuming that the fault plane of this earthquake consisted only of asperities, and the area outside the asperities was neglected. In the recipe for predicting ground motions of future crustal earthquakes developed by [Irikura and Miyake \(2011\)](#), the rupture plane was also divided into two parts with different stress drops, the asperities and the area outside the asperities.

In this article, we also assumed that the source of the target earthquake included only asperities, and we ignored the area outside the asperities, in contrast to [Kohrs-sansorny et al. \(2005\)](#). The seismic moment of the combined asperities accounts for 44% of the total seismic moment ([Somerville et al., 1999](#)). The averaged stress drop over the entire fault plane was estimated depending on the three-stage stress drop varying with the aspect ratio ([Dalguer et al., 2008](#)). Simultaneously considering the stress-drop ratio $\Delta\sigma_b/\Delta\sigma_a$ ($\Delta\sigma_b$, stress drop on the asperities; $\Delta\sigma_a$, stress drop outside the asperities) ([Dalguer et al., 2008](#)), and the combined area ratio $S_a/S = 0.22$ (S_a , the combined area of asperities; S , the rupture area) ([Somerville et al., 1999](#)), the stress drop on the asperities can be determined.

Ground-Motion Simulation for the M_w 6.6 Lushan Mainshock

Approximately 3000 aftershocks occurred within three days following the Lushan mainshock in a narrow area of 45 km multiplied by 20 km. The focal mechanisms and relocated hypocenter locations for some aftershocks were determined by [Lyu et al. \(2013\)](#), [Han et al. \(2014\)](#), and others. Most of the aftershocks occurred within the fault rupture plane, and the focal mechanisms are similar to the mainshock. A total of 1123 strong-motion recordings were collected by the National Strong-Motion Observation Network System of China during the Lushan aftershocks up to 6 July 2013. Nineteen $M_s \geq 4.0$ aftershocks were recorded by more than 20 strong-motion stations.

An M_w 4.4 earthquake that occurred on 20 April 2013 at 01:02:58 a.m. UTC, which was named EQI, had an adjacent hypocenter and a similar focal mechanism to the Lushan mainshock as shown in Table 1 ([Lyu et al., 2013](#)). The hypocenter distance between the two earthquakes is approximately 10.9 km. Both earthquakes were thrust fault earthquakes although EQI had a smaller dip angle. EQI was determined to be an approximately symmetrical rupture, with 52% of the rupture propagation in the N204.5°E direction using the same method as [Wen, Wang, and Ren \(2015\)](#). A total of 37 strong-motion stations obtained strong-motion recordings in EQI, of which 16 stations were also triggered in the Lushan mainshock (Fig. 1). The 16 stations are distributed evenly in the azimuth around the epicenter of the

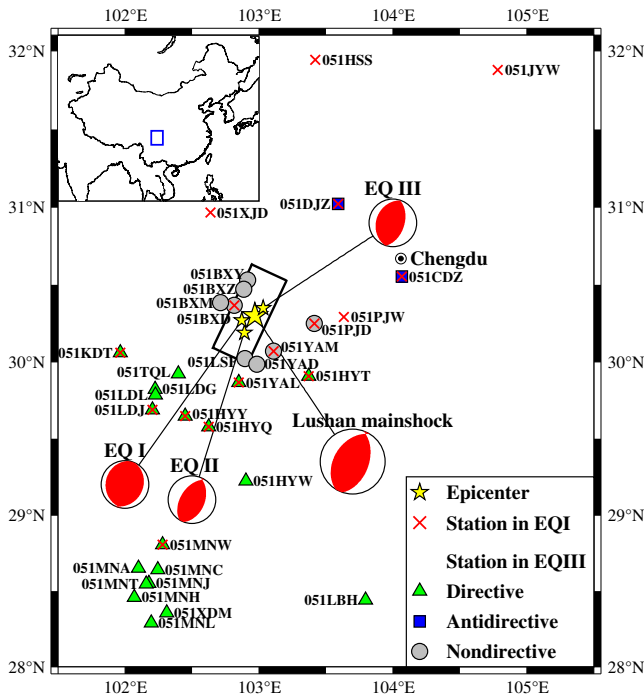


Figure 1. The strong-motion stations that recorded EQ I and EQ III, which were also triggered by the M_w 6.6 Lushan mainshock. Stations in EQ III are divided into three groups: directive, antidirective, and nondirective stations. The station codes are shown beside the stations. The rectangle represents the surface projection of the fault plane inverted by Wang *et al.* (2013). The color version of this figure is available only in the electronic edition.

Lushan mainshock. The hypocenter distances at most of the 16 stations are not greater than 150 km. Strong-motion recordings obtained by the 16 stations during the EQ I were regarded as EGFs for simulating ground motions of the M_w 6.6 Lushan earthquake. The baseline correction and a Butterworth band-pass filtering between 0.2 and 30 Hz were carried out.

According to the scaling relationship between the seismic moment and the rupture area (Somerville *et al.*, 1999), the Lushan mainshock ruptured an appropriately 445 km² area. In view of the thicker crust of approximately 50 km in this region, the aspect ratio of 1.0 may be appropriate for the Lushan mainshock (Shaw and Scholz, 2001). Following Dalguer *et al.* (2008), the averaged stress drop over the fault plane was estimated to be 1.5 MPa, which has coincidental consistency with the result given by Hao *et al.* (2013). If a single asperity lay on the fault plane of the Lushan mainshock, $\Delta\sigma_b/\Delta\sigma_a$ is equal to 0.1 (Dalguer *et al.*, 2008). The stress drop on the asperity was estimated to be 5.03 MPa on the foundation of $S_a/S = 0.22$ (Somerville *et al.*, 1999). According to the circular crack of Brune (1970) and the scaling relationship developed by Somerville *et al.* (1999), the stress drop of EQ I was calculated to be 2.31 MPa, which is close to the result of 2.05 MPa inverted by Wen, Wang, Ren, and Ji (2015). The stress drop ratio C was set to be 2.18.

The two-step stochastic EGF method was adopted to simulate the three-component acceleration time histories of the M_w 6.6 Lushan mainshock at 16 stations in 200 realizations. Each realization represents a unique source rupture process. All realizations constitute a sample set of various rupture processes. For each realization, we can estimate the rupture parameters by the method proposed by Convertito *et al.* (2012) using the simulated peak ground-motion parameters.

In this article, we focused on the simulated ground motions averaged over all realizations, which may result from a symmetrical rupture of the target earthquake. The simulated three-component acceleration time histories at each station, whose 5% damped pseudoabsolute response spectral acceleration (PSA) of the two horizontal components has the best fit to the arithmetically averaged PSA over the 200 realizations, were regarded as the averaged simulation, as shown in Figure 2. In general, the waveform and the shaking duration of the simulated accelerograms are in visually good agreement with the observed ones, although the peak ground acceleration (PGA) has some discrepancies. The simulated accelerograms of several near-field stations, such as 051BXD and 051YAM, are also performed well.

PGAs of the most observed recordings fall within the variation range of the simulated ground motions in the 200 realizations (Fig. 3). PGA is the geometric mean of the PGAs of the two orthogonal horizontal components (east–west and north–south). The simulated PGAs averaged over the 200 realizations have good consistency with the observed ones, for which the residuals ($\log[\text{PGA}_{\text{Obs.}}/\text{PGA}_{\text{Sim.}}]$) generally vary from -0.2 to 0.2 . The residuals do not show a significant correlation with the hypocenter distance.

Figure 3 also shows the PGAs predicted by the five Next Generation Attenuation-West2 (NGA-West2) models (ASK14, BSSA14, CB14, CY14, and I14) with the uniform weight (Abrahamson *et al.*, 2014; Boore *et al.*, 2014; Campbell and Bozorgnia, 2014; Chiou and Youngs, 2014; Idriss, 2014). The V_{S30} values were derived from the NGA-West 2 site database or inferred from the 20 m borehole data, except for two stations 051DJZ and 051JYW where data were not available. The rupture distance and the Joyner–Boore distance were calculated based on the fault plane provided by Wang *et al.* (2013). The predicted PGAs reproduce the observed values well at hypocenter distance $R_{\text{hyp}} < 150$ km, except for the PGA at station 051BXD, which was significantly affected by the local terrain (Wen and Ren, 2014). Residuals of the predicted PGAs are exposed at a similar level to the simulated ones, but are more scattered. The general underestimation of the predicted PGAs at larger distances may be related to the “High Q” in this region (Boore *et al.*, 2014). Compared with the predicted values, the simulated PGAs seem much better.

PSAs of the simulated ground motions in the 200 stochastic realizations are shown in Figure 4. The averaged PSA and the one standard deviation range were calculated to represent the variability of the simulated results. The simulated

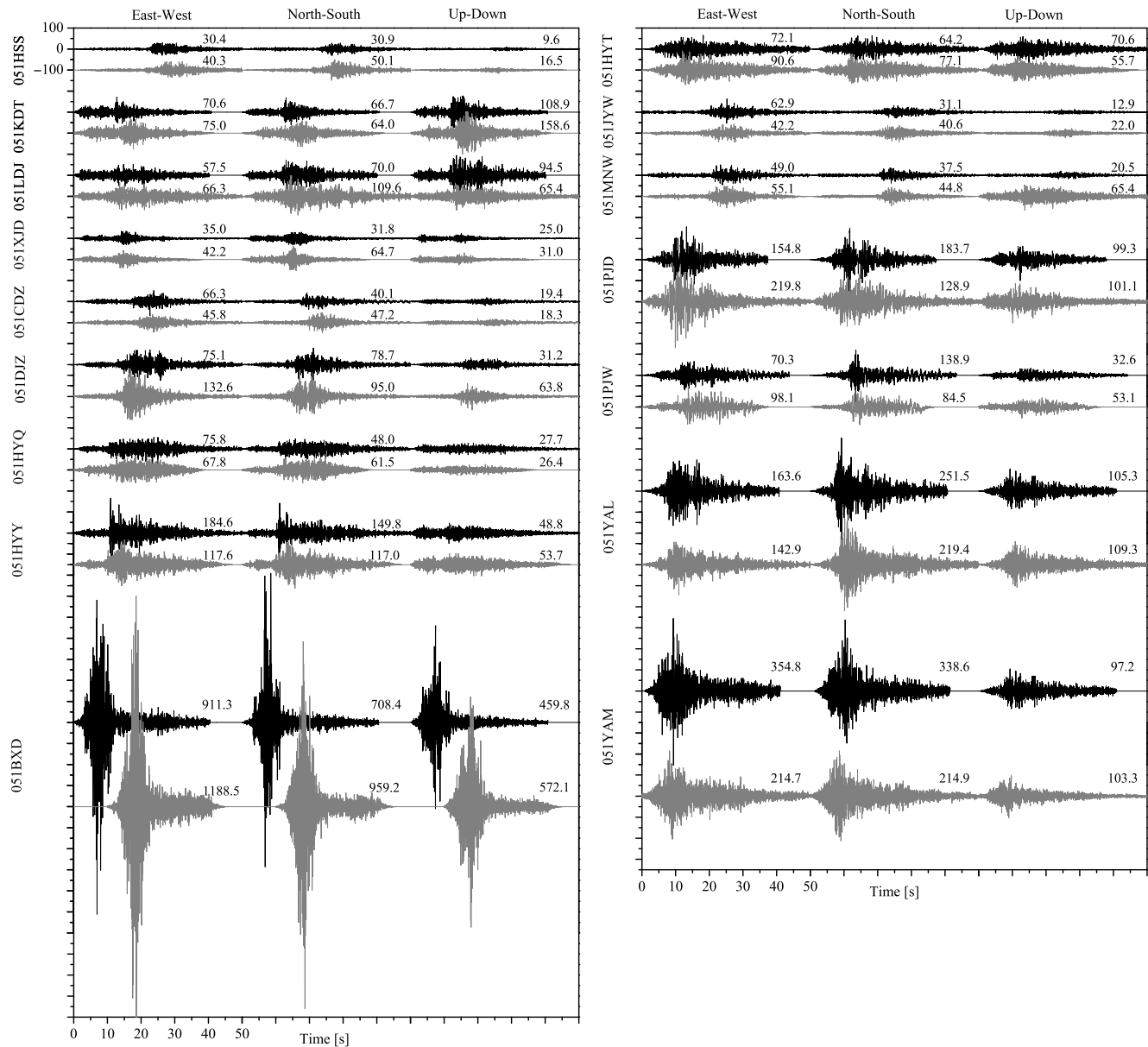


Figure 2. Comparisons of the simulated three-component acceleration time histories (gray) with the observed ones (dark). The numbers represent the peak ground accelerations (PGAs) in centimeters per square second.

PSAs show obvious variation in large ranges. The averaged simulated PSA is generally in good agreement with the observed values. The peak value, or the platform, of the PSA appears in similar periods for the simulated and observed recordings, which indicates the good representation of the site effects.

Residuals of the averaged simulated PSA ($\log[PSA_{Obs.}/PSA_{Sim.}]$) over the 200 realizations at each station and residuals averaged over all stations at some periods from 0.075 to 5 s are shown in Figure 5a. Residuals at intermediate periods from 0.15 to 2 s slightly fluctuate from 0 to 0.2, which indicates a slight underestimation of the observed recordings. At long periods (> 2.0 s), residuals rapidly increase with the increasing period, which is much

greater than zero. Simulated long-period ground motions are significantly lower than the observed values, which may be related to the EGFs from a small earthquake that lack long-period signals. However, the simulated ground motions are slightly higher at short periods (<0.15 s) whose residuals vary in a range from -0.2 to 0. Generally speaking, the short-period (<2.0 s) ground motions are successfully simulated with residuals within ± 0.2 . The averaged residuals over some periods from 0.075 to 5 s at each station all fluctuate approximately 0.2, as shown in Figure 5b, which indicates no dependency on the hypocenter distance.

Ground motions of the Lushan mainshock were successfully simulated using the two-step stochastic EGF method.

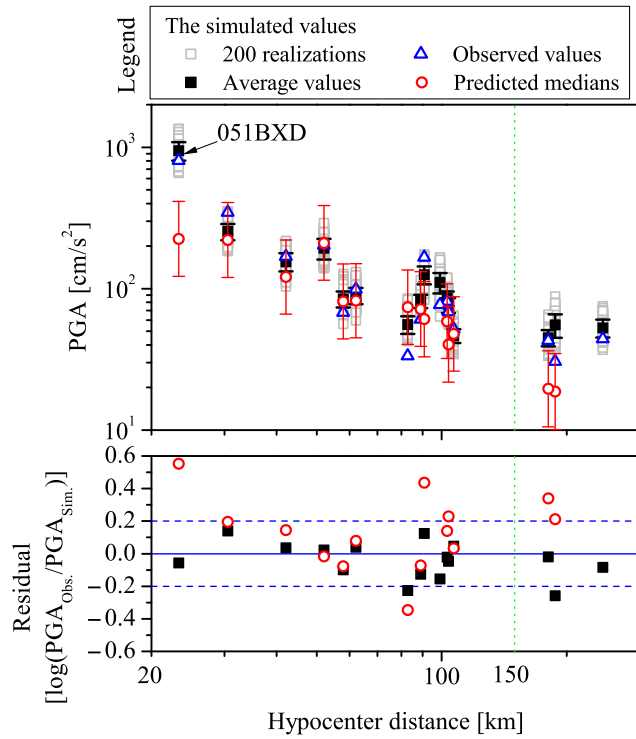


Figure 3. Comparison of the PGAs of the simulated ground motions with the observed recordings. The error bars represent the one standard deviation range of the simulated PGAs. Predicted medians and the one standard deviation range derived from the Next Generation Attenuation-West2 (NGA-West2) models with uniform weight are also compared. The bottom panel shows residuals of the simulated PGAs averaged over the 200 realizations and the predicted medians. The color version of this figure is available only in the electronic edition.

The symmetrical and concentrated rupture of the Lushan mainshock, as well as ground motions from a symmetrical rupture earthquake as EGFs, may contribute to the good reproductions. The validity of this method was proved.

Simulating the Rupture Directivity Effects

The rupture directivity changes the energy distribution over time, radiated by the source rupture at various azimuths. The duration of the apparent source time function (ASTF) is induced to vary with the azimuth of the observation station. In the direction of the rupture, the ASTF experiences a shorter duration, but a longer duration in the opposite direction. Converting the ASTF to the source spectrum in frequency domain, the azimuthal variation appears as higher spectral amplitudes at higher frequencies in the direction of the rupture and a lack of such high-frequency signals in the opposite direction. This can be described by the azimuthal variation of the apparent corner frequency f_a . For a simple homogeneous kinematic line source model that ruptures unilaterally with a uniform slip and constant rupture velocity v_r (Ben-Menahem, 1961):

$$f_a = \sqrt{f_S \times f_L} = \sqrt{\frac{2}{T_S} \times \frac{2v_r}{L} \frac{1}{1 - \frac{v_r}{\beta} \cos \psi}} = f_c \sqrt{\frac{1}{1 - \frac{v_r}{\beta} \cos \psi}} = f_c D, \quad (3)$$

in which f_S and f_L represent the corner frequencies related to the source time function and the source finiteness factor, respectively. T_S is the rise time of the source time function. ψ is the azimuth measured from the direction of the rupture to the observation station. L is the length of the rupture plane. The correction coefficient D represents the adjustment of the true corner frequency f_c for f_a . Furthermore, for an asymmetric bilateral rupture with a proportion k of the rupture length in the direction of the predominant rupture accounting for the whole rupture length:

$$D = \left[\left(\frac{k^2}{1 - \frac{v_r}{\beta} \cos \psi} \right) + \left(\frac{(1-k)^2}{1 + \frac{v_r}{\beta} \cos \psi} \right) \right]^{1/4}. \quad (4)$$

Owing to the change in apparent corner frequency at different observation stations, parameters N and C in equation (2) both change. Two new parameters N_a and C_a substitute for N and C :

$$N_a = ND^n, \quad C_a = CD^{-3n}. \quad (5)$$

n is equal to 1 or -1 . If $n = 1$, the rupture directivity of the small earthquake taken as EGF is considered; if $n = -1$, the rupture directivity of the target earthquake is considered. Meanwhile, the probability density functions ρ_c and ρ_d also change.

The characteristics of the rupture propagation of four larger Lushan aftershocks have been inverted using peak ground-motion parameters by Wen, Wang, and Ren (2015). Two of the four aftershocks that occurred on 20 April 2013 at 03:34:17 UTC (EQII), and 20 April 2013 at 20:53:44 UTC (EQIII) predominantly rupture toward the southwest, approximately in the direction of N210°E. The other two aftershocks rupture approximately symmetrically. EQII and EQIII both show significant rupture directivity, but EQIII is much stronger. EQII and EQIII have similar thrust fault mechanisms to the Lushan mainshock (Table 1). The Lushan mainshock is located to the northeast of EQII by approximately 14.5 km, but southwest of EQIII by approximately 8.1 km (Fig. 1). EQII and EQIII both triggered 53 strong-motion stations, most of which were the same. Owing to the similarity of the rupture directivity and the triggered stations for EQII and EQIII, no matter which one can be used as the EGF. Herein, strong-motion recordings obtained at 29 stations (Fig. 1), which were both triggered in EQIII and the Lushan mainshock, were regarded as EGFs to simulate the Lushan mainshock. EQIII was measured as M_w 4.5 (Lyu *et al.*, 2013). The stress drop of EQIII was also set to 2.31 MPa according to the circular crack of Brune (1970) and the scaling relationship developed by Somerville *et al.*

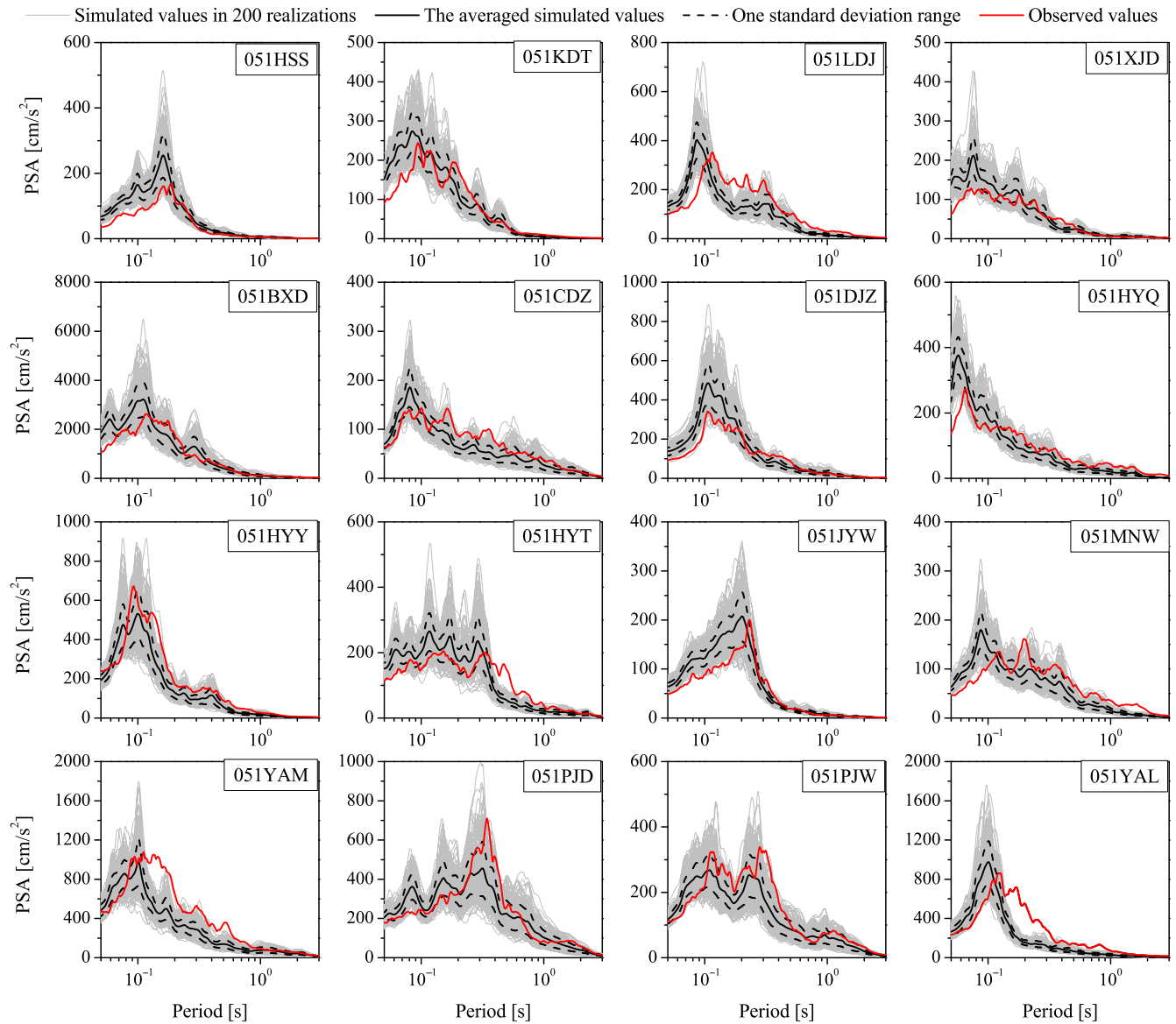


Figure 4. The 5% damped pseudoabsolute response spectral accelerations (PSAs) of the simulated and observed ground motions. The dark solid line and the dashed line represent the averaged simulated PSA and the one standard deviation range, respectively. The color version of this figure is available only in the electronic edition.

(1999), which is close to the result of 1.92 MPa estimated by Wen, Wang, Ren, and Ji (2015).

We simulated ground motions of the M_w 6.6 Lushan mainshock in 200 realizations in two cases. In the first case, the rupture directivity of EQIII was not considered. A constant f_c was adopted. The second case was that azimuthal f_a was adopted to consider the rupture directivity. A strike-normal line, which is perpendicular to the strike and across the epicenter of EQIII, divides stations into three groups, including the directive stations in the predominant rupture direction, antidirective stations in the opposite direction of the predominant rupture, and nondirective stations close to the division line, as shown in Figure 1. Some stations very close to the surface fault projection of the fault plane of the Lushan main-

shock were also assigned to nondirective stations owing to the complicated impacts of the rupture process. Only two stations 051CDZ and 051DJZ were assigned as antidirective stations, and their hypocenter distances are appropriately 100 km.

In the first case, PGAs of the simulated ground motions at directive stations are generally much higher than the observed values and the predicted medians from the NGA-West2 models, even exceeding the one standard deviation range of the predicted values (Fig. 6a). Conversely, the simulated PGA at the antidirective station 051CDZ is lower than the observed value and the predicted median, but falls within the one standard deviation range of the predicted values. The observed PGAs, or the predicted medians, are exactly in the middle of the simulated values between the directive and

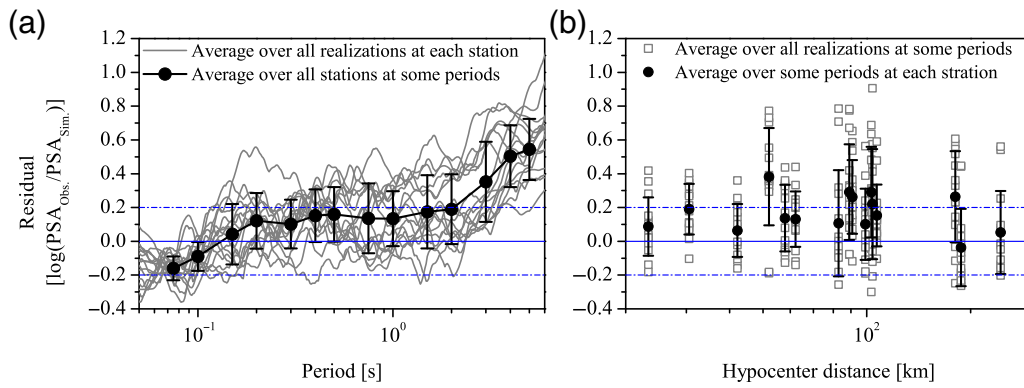


Figure 5. (a) Residuals of the averaged simulated PSAs over the 200 realizations at each station and the averaged residuals at some periods over all stations; (b) residuals of the averaged simulated PSAs over the 200 realizations at some periods and the averaged residuals over these periods at each station. Error bars represent the one standard deviation range. The color version of this figure is available only in the electronic edition.

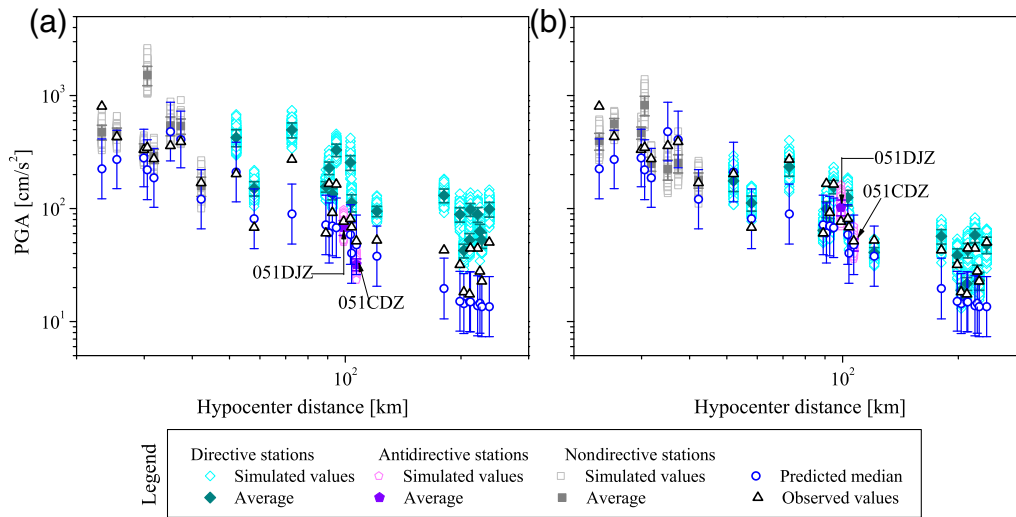


Figure 6. Comparison of the PGAs of the simulated recordings in the 200 realizations in the (a) first and (b) second cases with the observed values and the predicted medians from the five NGA-West2 models with uniform weight. Error bars represent one standard deviation range. The color version of this figure is available only in the electronic edition.

antidirective stations, which may be ascribed to the rupture directivity of EQIII. The simulated PGAs at most of the non-directive stations are in good agreement with the observed and predicted values.

In the second case, the simulated PGAs significantly decrease at directive stations, but increase at antidirective stations (Fig. 6b). The simulated PGAs are in good agreement with the observed values. Most of the simulated PGAs fall within the one standard deviation range of the predicted values, except for recordings at a large hypocenter distance (≥ 200 km).

The antidirective station 051CDZ and four directive stations (051LDG, 051LDJ, 051LDL, and 051KDT) have the similar hypocenter distance of approximately 100 km. The east–west components of the observed recordings at these stations have similar amplitudes (Fig. 7). In the first case, the simulated accelerograms at the four directive stations are

significantly larger than observed recordings, whereas the opposite is the case at station 051CDZ. The simulated recordings have large discrepancies with the observed ones. In the second case, the amplitudes of the simulated accelerograms dramatically decrease at the four directive stations, whereas they slightly increased at antidirective station 051CDZ. The simulated recordings provide good reproductions of the observed ones.

In the first case, PSAs of the observed recordings are significantly lower than the simulated values in the 200 realizations at directive stations and, conversely, greater than the averaged simulated values at antidirective stations, as shown in Figure 8. In the second case, PSAs of the simulated recordings sharply decline to match the observed values well at directive stations while essentially enlarging at antidirective stations, also providing a better reproduction.

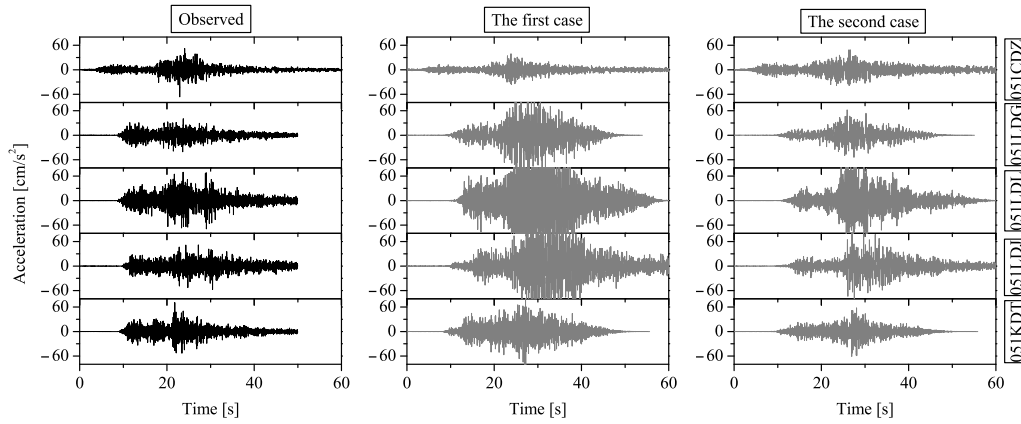


Figure 7. The observed and simulated acceleration time histories of the east–west components at the antidirective station 051CDZ and four directive stations with similar hypocenter distances.

Residuals of the averaged simulated PSA ($\log[\text{PSA}_{\text{Obs.}}/\text{PSA}_{\text{Sim.}}]$) over the 200 realizations at each station and the averaged residuals at some periods from 0.075 to 5 s for directive, antidirective, and nondirective stations in the two cases are shown in Figure 9. When we neglect the directivity, residuals in short periods (< 2.0 s) are generally less than zero at directive stations, greater than zero at antidirective stations, and close to zero at nondirective stations. The smaller the period, the less the residual. However, residuals of the simulated long-period (> 2.0 s) ground motions are all greater than zero regardless of where the stations are located. After considering the directivity, residuals in long periods (> 2.0 s) do not show obvious changes, still much greater than zero, which may be related to the lack of the long-period signal for EGFs from the small earthquake. However, significant changes can be observed in short periods (< 2.0 s). Residuals increase to nearly zero at directive stations yet essentially decrease at antidirective stations.

Comparisons of the simulated ground motions in the two cases clearly show that the rupture directivity of EQIII exposes significant impacts on PGAs and short-period PSAs (< 2.0 s) of the simulated recordings, especially at directive stations. The high-frequency rupture directivity is well simulated using the azimuthal apparent corner frequency in the two-step stochastic EGF method.

Simulating the Directivity Effects of the Target Earthquake

A series of M_w 6.6 Lushan-like earthquakes were used as examples. These earthquakes rupture along the same blind-thrust fault oriented at $N210^\circ\text{E}$ with a constant rupture velocity of approximately 2.0 km/s, the same as the Lushan mainshock (Hao *et al.*, 2013). The Lushan mainshock did not show significant directivity effects (Zhang *et al.*, 2013). However, these Lushan-like earthquakes were assumed to show different rupture directivities. The rupture proportion k in the direction of $N30^\circ\text{E}$ was set to be 1.0, 0.8, 0.6, 0.5, 0.4, 0.2, and 0, respectively. For example, if $k = 1$, the rup-

ture length in the direction of $N30^\circ\text{E}$ is the whole rupture length. The correction coefficient D was derived from equation (4) to adjust the corner frequency for the apparent corner frequency. New parameters N_a and C_a substituting for N and C in equation (2) are derived from the equation (5) with $n = -1$.

Recordings obtained at 16 stations (Fig. 1) in EQI were adopted as EGFs to simulate the ground motions of these Lushan-like earthquakes in 200 realizations. The 16 stations were divided into three parts according to the locations of these stations, of which 6 stations (051HSS, 051XJD, 051CDZ, 051DJZ, 051JYW, and 051PJW) toward the northeast are classified as northeast stations, 8 stations (051KDT, 051LDJ, 051HYQ, 051HYY, 051HYT, 051YAL, 051MNW, and 051YAM) toward the southwest as southwest stations, and 2 stations (051BXD and 051PJD) as center stations. We observed strong-motion recordings from the Lushan mainshock as the actual ground motions without directivity effects.

Residuals of the PGAs of the simulated recordings averaged over southwest and northeast stations for different k are shown in Figure 10. The residuals averaged over northeast stations gradually increase from negative values to positive values with decreasing k from one to zero, which indicates a decreasing trend of the simulated ground motions from greater than the observed values to lower than the observed values. An opposite gradually increasing tendency of the simulated ground motions is observed at southwest stations. PGAs of the simulated ground motions at a station, which changes gradually from the front to the backside of the predominant rupture with the varied k , decrease gradually. Residuals of PSAs at different periods also show similar variation to the PGA (Fig. 11). However, the simulated ground motions at southwest stations in periods from 0.5 to 2 s are generally lower than the observed values. The similar underestimation was also observed in the simulated ground motions of the Lushan mainshock in these periods (Fig. 5). Variations of the residuals with different k described above indicate that the simulated ground motions show

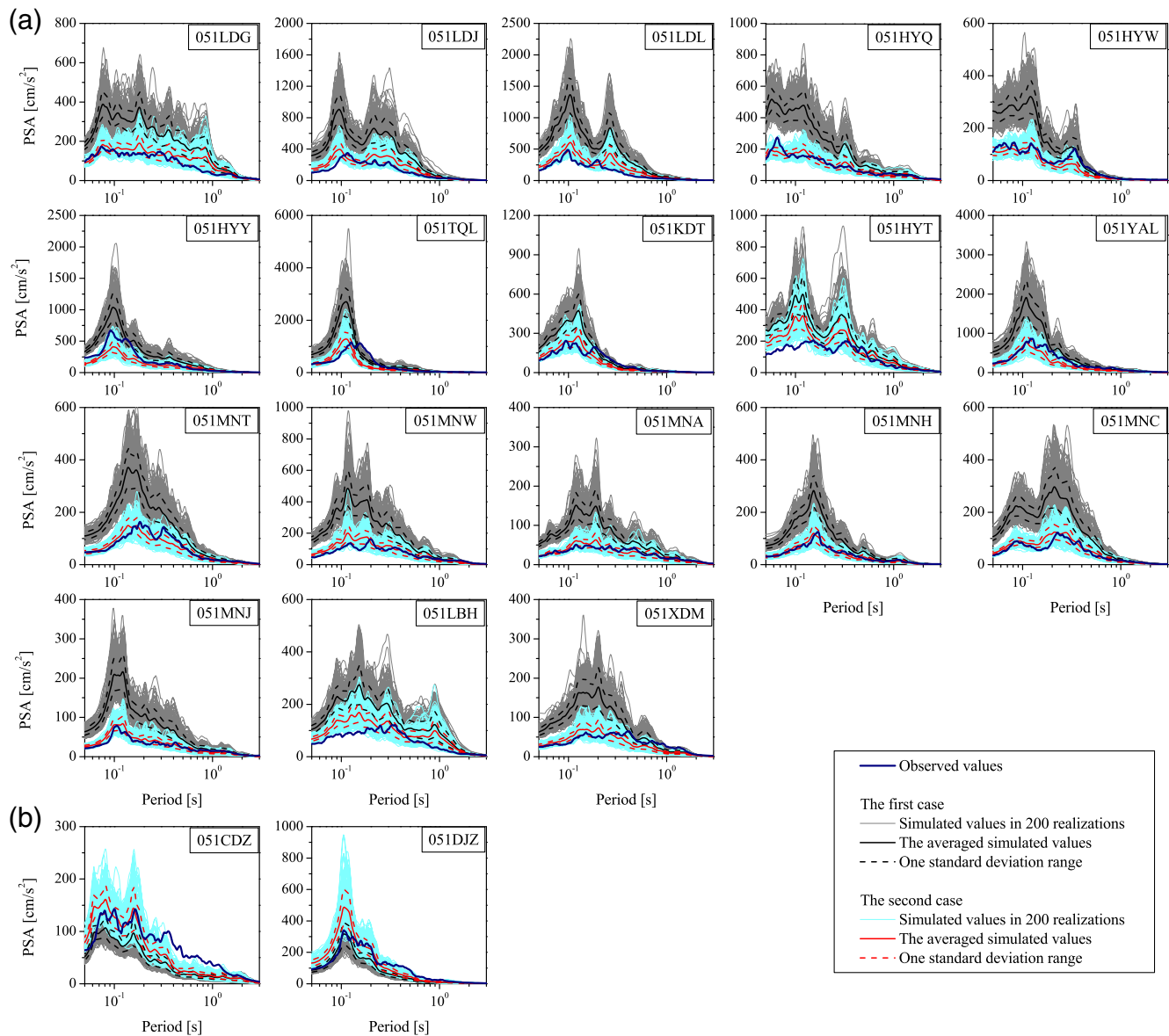


Figure 8. Comparisons of the 5% damped PSAs of the simulated recordings from both cases with the observed recordings. The average and one standard deviation range for both cases are shown to represent variability. The station name is shown in the top-right corner of each panel. (a) Directive station and (b) antidirective station. The color version of this figure is available only in the electronic edition.

significant directivity effects and more severe ground motions in the direction of the predominant rupture.

Conclusion

The two-step stochastic EGF method proposed by Kohrs-Sansorny *et al.* (2005) was used to simulate ground motions of the 2013 M_w 6.6 Lushan mainshock in 200 realizations, taking 16 strong-motion recordings from an M_w 4.4 earthquake (EQI) with approximately symmetrical rupture as EGFs. To reflect the highly nonuniform distribution of the stress drop on the fault plane, the source of the Lushan mainshock was set to consist only of an asperity which was determined by the statistical scaling relations. The simulated ground motions

averaged over the 200 realizations, which may result from a symmetrical rupture, are in good agreement with the observed recordings at short periods (< 2.0 s). The symmetrical and concentrated source rupture of the Lushan mainshock may contribute to the good consistency. However, simulated long-period (> 2.0 s) ground motions are significantly lower than the observed values. This may be related to the EGFs from a small earthquake with a limited source size that lacks long-period signals. The good reproductions of ground motions produced by the Lushan mainshock prove the validity of the method used in this study.

Observed recordings from an M_w 4.5 earthquake (EQIII) with significant rupture directivity were used as EGFs to investigate the directivity effects on the simulated ground

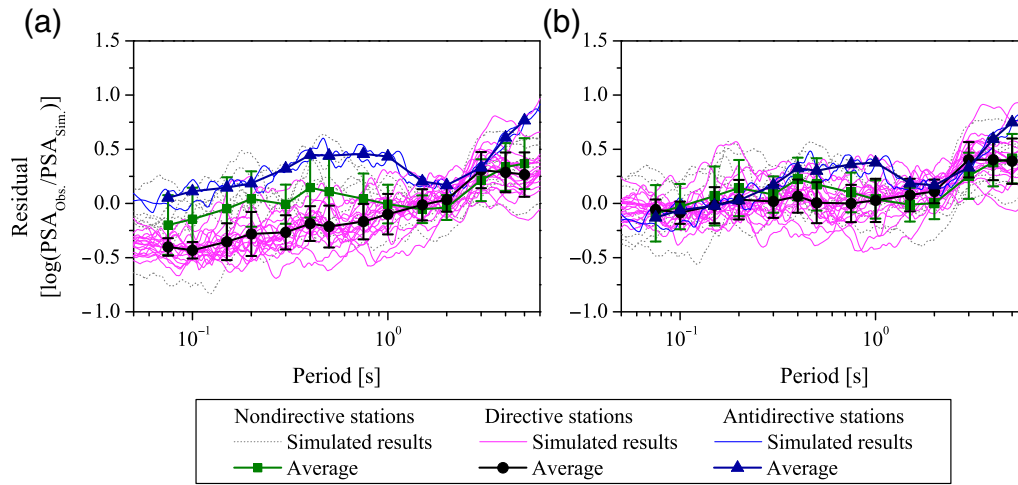


Figure 9. Residuals of the averaged simulated PSAs over the 200 realizations at each station and the averaged residuals at some periods for directive, antidirective, and nondirective stations in the (a) first and (b) second cases. The color version of this figure is available only in the electronic edition.

motions of the Lushan mainshock. The results indicated that rupture directivity mainly exerts significant influences on simulated short-period (< 2.0 s) ground motions, which are responsible for the large discrepancies with the observed values. More obvious effects can be observed in the shorter period. Simulated ground motions at directive stations are much higher than the observed ones, whereas the opposite is true at antidirective stations. More significant impacts are exposed on ground motions at directive stations. Adopting a correction coefficient D to adjust the apparent corner frequency f_a at each station, we succeed in simulating the rupture directivity of EQIII on the short-period (< 2.0 s) ground motions. The observed recordings are reproduced well.

Ground motions produced by a series of M_w 6.6 Lushan-like earthquakes with different rupture directivities

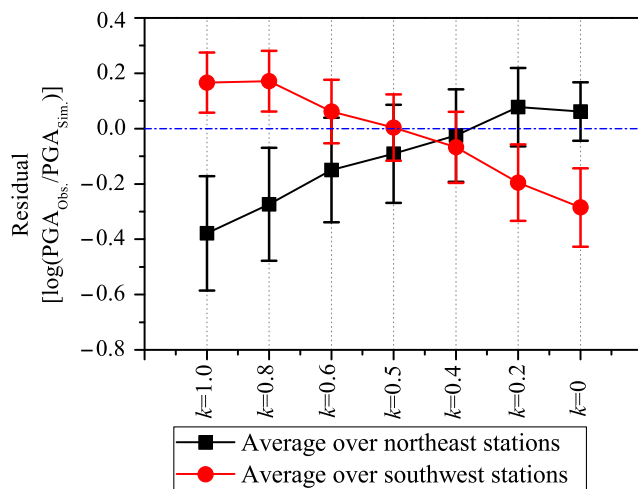


Figure 10. The averaged residuals of peak ground motions (PGAs) of the simulated ground motion over the northeast and southwest stations for a series of Lushan-like earthquakes with different k . The color version of this figure is available only in the electronic edition.

were simulated using the azimuthal apparent corner frequency. When a station changes from the front to the backside of the predominant rupture, the simulated ground motions at this station gradually decrease. The simulated ground motions show the significant directivity effects, where more severe ground motions are generated at directive stations. Our results indicate that directivity effects can be simulated in the two-step stochastic EGF method by adopting varied apparent corner frequencies with azimuth or station location. The two-step stochastic EGF method can provide good reproductions for future earthquakes, especially when the directivity effects are well simulated.

In this article, the statistical scaling relations for earthquakes were adopted to determine the averaged stress drop, assuming that earthquakes follow self-similarity. The scaling relations pay more attention to the commonness of large numbers of earthquakes rather than the individuality of a certain earthquake. Uncertainty must be inevitable owing to the significant change in the stress drop. Meanwhile, scaling relations between the seismic moment and rupture area were regionally variable (Dowrick and Rhoades, 2004). Therefore, the averaged stress drop derived from the statistic scaling relations may have large variability. However, the variability was not investigated in this article.

Data and Resources

Strong-motion recordings used in this article were obtained from the China Strong-Motion Networks Center at <http://www.csmnc.net/> (last accessed December 2013). V_{S30} measurements were obtained from the Next Generation Attenuation (NGA) site database of the Pacific Earthquake Engineering Research (PEER) Center at <http://peer.berkeley.edu/nga/> (last accessed March 2014). Some of the plots were produced using Generic Mapping Tools (Wessel and Smith, 1991).

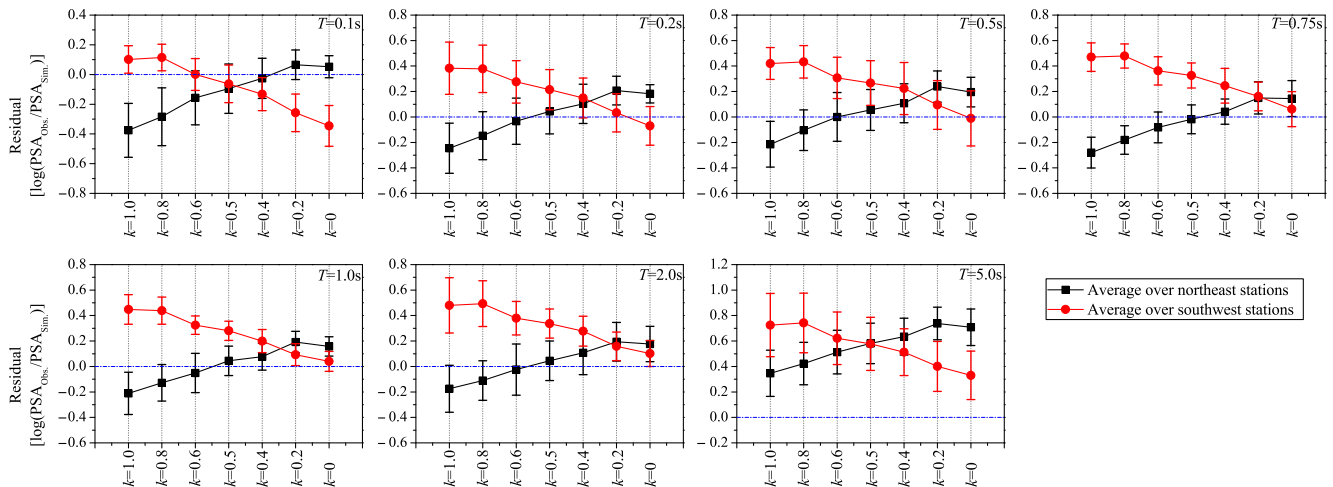


Figure 11. The averaged residuals of the 5% damped PSAs of the simulated ground motions over the northeast and southwest stations for a series of Lushan-like earthquakes with different k . The color version of this figure is available only in the electronic edition.

Acknowledgments

We are very grateful to the reviewers for providing valuable comments, which helped improve the article. This work has been supported by the Scientific Research Fund of the Institute of Engineering Mechanics, China Earthquake Administration (CEA) Number 2016A04, Nonprofit Industry Research Project of CEA under Grant Number 201508005, and Chinese National Natural Science Fund Grants Number 51308515.

References

- Abrahamson, N. A., W. J. Silva, and R. Kamai (2014). Summary of the ASK14 ground-motion relation for active crustal regions, *Earthq. Spectra* **30**, 1024–1056.
- Allmann, B., and P. M. Shearer (2009). Global variations of stress drop for moderate to large earthquakes, *J. Geophys. Res.* **114**, no. B01310, doi: [10.1029/2008JB005821](https://doi.org/10.1029/2008JB005821).
- Ben-Menahem, A. (1961). Radiation of seismic surface waves from finite moving sources, *Bull. Seismol. Soc. Am.* **51**, 401–435.
- Bernard, P., A. Herrero, and C. Berge (1996). Modeling directivity of heterogeneous earthquake ruptures, *Bull. Seismol. Soc. Am.* **86**, 1149–1160.
- Boatwright, J. (2007). The persistence of directivity in small earthquakes, *Bull. Seismol. Soc. Am.* **97**, 1850–1861.
- Boore, D. M., J. P. Stewart, E. Seyhan, and G. M. Atkinson (2014). NGA-West 2 equations for predicting PGA, PGV, and 5%-damped PSA for shallow crustal earthquakes, *Earthq. Spectra* **30**, 1057–1086.
- Brune, J. N. (1970). Tectonic stress and the spectra of seismic shear waves from earthquakes, *J. Geophys. Res.* **75**, 4997–5009.
- Campbell, K. W., and Y. Bozorgnia (2014). NGA-West 2 ground motion model for the average horizontal components of PGA, PGV, and 5%-damped linear acceleration response spectra, *Earthq. Spectra* **30**, 1087–1116.
- Chiou, B. S. J., and R. R. Youngs (2014). Update of the Chiou and Youngs NGA model for the average horizontal component of peak ground motions and response spectra, *Earthq. Spectra* **30**, 1117–1154.
- Convertito, V., and A. Emolo (2012). Investigating rupture direction for three 2012 moderate earthquakes in northern Italy from inversion of peak ground-motion parameters, *Bull. Seismol. Soc. Am.* **102**, 2764–2770.
- Convertito, V., M. Caccavale, R. D. Matteis, A. Emolo, D. Wald, and A. Zollo (2012). Fault extent estimation for near-real-time ground-shaking map computation purposes, *Bull. Seismol. Soc. Am.* **102**, 661–679.
- Courboux, F., J. Converset, J. Balestra, and B. Delouis (2010). Ground-motion simulations of the 2004 M_w 6.4 Les Saintes, Guadeloupe, earthquake using ten smaller events, *Bull. Seismol. Soc. Am.* **100**, 116–130.
- Courboux, F., A. Dujardin, M. Vallee, B. Delouis, C. Sira, A. Deschamps, L. Honore, and F. Thouvenot (2013). High-frequency directivity effect for an M_w 4.1 earthquake, widely felt by the population in southeastern France, *Bull. Seismol. Soc. Am.* **103**, 3347–3353.
- Courboux, F., M. Vallee, M. Causse, and A. Chounet (2016). Stress-drop variability of shallow earthquakes extracted from a global database of source time functions, *Seismol. Res. Lett.* **87**, 912–918.
- Cultrera, G., F. Pacor, G. Franceschina, A. Emolo, and M. Cocco (2009). Directivity effects for moderate-magnitude earthquakes (M_w 5.6–6.0) during the 1997 Umbria-Marche sequence, central Italy, *Tectonophysics* **476**, 110–120.
- Dalguer, L. A., H. Miyake, S. M. Day, and K. Irikura (2008). Rupturing and buried dynamic-rupture models calibrated with statistical observations of past earthquakes, *Bull. Seismol. Soc. Am.* **98**, 1147–1161.
- Dowrick, D. J., and D. A. Rhoades (2004). Relations between earthquake magnitude and fault rupture dimensions: How regionally variable are they, *Bull. Seismol. Soc. Am.* **94**, 776–788.
- Fujii, Y., and M. Matsuura (2000). Regional difference in scaling laws for large earthquakes and its tectonic implication, *Pure Appl. Geophys.* **157**, 2283–2301.
- Gallovic, F., and J. Burjanek (2007). High-frequency directivity in strong ground motion modeling methods, *Ann. Geophys.* **50**, 203–211.
- Han, L. B., X. F. Zeng, C. S. Jiang, S. D. Ni, H. J. Zhang, and F. Long (2014). Focal mechanics of the 2013 M_w 6.6 Lushan, China earthquake and high-resolution aftershock relocations, *Seismol. Res. Lett.* **85**, 8–14.
- Hanks, T. C., and W. H. Bakun (2002). A bilinear source-scaling model for $M - \log A$ observations of continental earthquakes, *Bull. Seismol. Soc. Am.* **92**, 1841–1846.
- Hao, J. L., C. Ji, W. M. Wang, and Z. X. Yao (2013). Rupture history of the 2013 M_w 6.6 Lushan earthquake constrained with local strong motion and teleseismic body and surface waves, *Geophys. Res. Lett.* **40**, 5371–5376.
- Hartzell, S. H. (1978). Earthquake aftershocks as Green's functions, *Geophys. Res. Lett.* **5**, 1–4.
- Honore, L., F. Courboux, and A. Souriau (2011). Ground motion simulations of a major historical earthquake (1660) in the French

- Pyrenees using recent moderate size earthquakes, *Geophys. J. Int.* **187**, 1001–1018.
- Idriss, I. M. (2014). An NGA-West 2 empirical model for estimating the horizontal spectral values generated by shallow crustal earthquakes, *Earthq. Spectra* **30**, 1155–1178.
- Irikura, K. (1983). Semi-empirical estimation of strong ground motions during large earthquakes, *Bull. Disast. Prev. Res. Inst., Kyoto Univ.* **33**, 63–104.
- Irikura, K., and K. Kamae (1994). Estimation of strong ground motion in broad-frequency band based on a seismic source scaling model and an empirical Green's function technique, *Ann. Geophys.* **37**, 1721–1743.
- Irikura, K., and H. Miyake (2011). Recipe for predicting strong ground motion from crustal earthquake scenarios, *Pure Appl. Geophys.* **168**, 85–104.
- Irikura, K., H. Miyake, T. Iwata, K. Kamae, H. Kawabe, and L. A. Dalguer (2004). Recipe for predicting strong ground motion from future large earthquake, *Proc. of the 13th World Conference on Earthquake Engineering No. 1371*, Vancouver, Canada, 1–6 August.
- Joyner, W. B., and D. M. Boore (1986). On simulating large earthquakes by Green's function addition of smaller earthquakes, in *Earthquake Source Mechanics, Geophysical Monograph*, American Geophysical Union, Vol. 37, 269–274.
- Kamae, K., and H. Kawabe (2004). Source model composed of asperities for the 2003 Tokachi-Oki, Japan, earthquake ($M_{JMA} = 8.0$) estimated by the empirical Green's function method, *Earth Planets Space* **56**, 323–327.
- Kanamori, H. (1994). Mechanics of earthquakes, *Ann. Rev. Earth Planet. Sci.* **22**, 207–237.
- Kanamori, H., and D. L. Anderson (1975). Theoretical basis of some empirical relations in seismology, *Bull. Seismol. Soc. Am.* **65**, 1073–1095.
- Kohrs-Sansorny, C., F. Courboux, M. Bour, and A. Deschamps (2005). A two-stage method for ground motion simulation using stochastic summation of small earthquakes, *Bull. Seismol. Soc. Am.* **95**, 1378–1400.
- López-Comino, J. Á., F. de Lis Mancilla, J. Morales, and D. Stich (2012). Rupture directivity of the 2011, M_w 5.2 Lorca earthquake (Spain), *Geophys. Res. Lett.* **39**, L03301, doi: [10.1029/2011GL050498](https://doi.org/10.1029/2011GL050498).
- Lyu, J., X. S. Wang, J. R. Su, S. L. Pan, Z. Li, L. W. Yin, X. F. Zeng, and H. Deng (2013). Hypocenter location and source mechanism of the M_s 7.0 Lushan earthquake sequence, *Chin. J. Geophys.* **56**, 1753–1763 (in Chinese).
- McGuire, J. J. (2004). Estimating finite source properties of small earthquake ruptures, *Bull. Seismol. Soc. Am.* **94**, 377–393.
- McGuire, J. J., L. Zhao, and T. H. Jordan (2002). Predominance of unilateral rupture for a global catalog of large earthquakes, *Bull. Seismol. Soc. Am.* **92**, 3309–3317.
- Miyake, H., T. Iwata, and K. Irikura (2003). Source characterization for broadband ground-motion simulation: Kinematic heterogeneous source model and strong motion generation area, *Bull. Seismol. Soc. Am.* **93**, 2531–2545.
- Murotani, S., S. Matsushima, T. Azuma, K. Irikura, and S. Kitagawa (2015). Scaling relations of source parameters of earthquakes occurring on inland crustal mega-fault systems, *Pure Appl. Geophys.* **172**, 1371–1381.
- Olsen, K. B., R. Madariage, and R. J. Archuleta (1997). Three-dimensional dynamic simulation of the 1992 Landers earthquake, *Science* **278**, 834–837.
- Ordaz, M., J. Arboleda, and S. K. Singh (1995). A scheme of random summation of an empirical Green's function to estimate ground motions from future large earthquakes, *Bull. Seismol. Soc. Am.* **85**, 1635–1647.
- Ruiz, J. A., D. Baumont, P. Bernard, and C. Berge-Thierry (2011). Modeling directivity of strong ground motion with a fractal, k^{-2} , kinematic source model, *Geophys. J. Int.* **186**, 226–244.
- Shaw, B. E., and C. H. Scholz (2001). Slip-length scaling in large earthquakes: Observation and theory and implications for earthquake physics, *Geophys. Res. Lett.* **28**, 2995–2998.
- Somerville, P., K. Irikura, R. Graves, S. Sawada, D. Wald, N. Abrahamson, Y. Iwasaki, T. Kagawa, N. Smith, and A. Kowada (1999). Characterizing crustal earthquake slip models for the prediction of strong ground motion, *Seismol. Res. Lett.* **70**, 59–80.
- Wang, W. M., J. L. Hao, and Z. X. Yao (2013). Preliminary result for rupture process of Apr. 20, 2013, Lushan earthquake, Sichuan, China, *Chin. J. Geophys.* **56**, 1412–1417 (in Chinese).
- Wells, D. L., and K. J. Coppersmith (1994). New empirical relationships among magnitude, rupture length, rupture width, rupture area, and surface displacement, *Bull. Seismol. Soc. Am.* **84**, 102–974.
- Wen, R. Z., and Y. F. Ren (2014). Strong-motion observations of the Lushan earthquake on 20 April 2013, *Seismol. Res. Lett.* **85**, 1043–1055.
- Wen, R. Z., H. W. Wang, and Y. F. Ren (2015). Rupture directivity from strong-motion recordings of the 2013 Lushan aftershocks, *Bull. Seismol. Soc. Am.* **105**, 3068–3082.
- Wen, R. Z., H. W. Wang, Y. F. Ren, and K. Ji (2015). Estimation of source parameters and quality factor based on generalized inversion method in Lushan earthquake, *J. Harbin Inst. Technol.* **47**, no. 4, 58–63 (in Chinese).
- Wennerberg, L. (1990). Stochastic summation of empirical Green's functions, *Bull. Seismol. Soc. Am.* **80**, 1418–1432.
- Wessel, P., and W. H. F. Smith (1991). Free software helps map and display data, *Eos Trans. AGU* **72**, 441.
- Zeng, Y. H., J. G. Anderson, and G. Yu (1994). A composite source model for computing realistic synthetic strong ground motions, *Geophys. Res. Lett.* **21**, 725–728.
- Zhang, Y., R. J. Wang, Y. T. Chen, L. S. Xu, F. Du, M. P. Jin, H. W. Tu, and T. Dahm (2014). Kinematic rupture model and hypocenter relocation of the 2013 M_w 6.6 Lushan earthquake constrained by strong-motion and teleseismic data, *Seismol. Res. Lett.* **85**, 15–22.
- Zhang, Y., L. S. Xu, and Y. T. Chen (2013). Rupture process of the Lushan 4.20 earthquake and preliminary analysis on the disaster-causing mechanism, *Chin. J. Geophys.* **56**, 1408–1411 (in Chinese).
- Zhao, C. P., Z. L. Chen, W. Hua, Q. C. Wang, Z. X. Li, and S. H. Zheng (2011). Study on source parameters of small to moderate earthquakes in the main seismic active regions, China mainland, *Chin. J. Geophys.* **54**, 1478–1489 (in Chinese).

Institute of Engineering Mechanics
 China Earthquake Administration
 Key Laboratory of Earthquake Engineering and Engineering Vibration of
 China Earthquake Administration
 No. 29 Xuefu Road
 Harbin 150080, China
 ruizhi@iem.ac.cn
 whw1990413@163.com
 renyefei@iem.net.cn